

Characterizing Scatter Correction Software of 5 Mobile Radiography Units

An Anthropomorphic Phantom Study

Tim Gossye, MSc,* Dimitri Buytaert, MSc,† Peter V. Smeets, MD,‡ Lieve Morbée, MD,‡ Elke Vereecke, MD,‡ Eric Achten, PhD, MD,‡ and Klaus Bacher, PhD*

Objectives: Bedside radiographs are usually obtained gridless, without a physical scatter correction grid because of several limitations. Therefore, multiple manufacturers of mobile radiography systems provide the possibility to apply scatter correction software (SC SW) on those images. The purpose of this study was to characterize different series of radiographs—gridless, SC SW, and physical grid—with an image quality assessment algorithm (IQAA). Furthermore, we investigated the potential dose reduction and the correlation between the output of the IQAA and the human observers.

Materials and Methods: We obtained different series of radiographs with an anthropomorphic phantom (multipurpose chest phantom N1 “Lungman,” Kyoto Kagaku, Kyoto, Japan). All radiographs were obtained with flat-panel detectors of 5 different manufacturers in a wall bucky system. An IQAA to analyze the radiographs was implemented in our department but was originally developed by the research group of the Duke University Medical Center. Seven physical quantities were calculated by the IQAA: rib-lung contrast ($RL_{contrast}$), subdiaphragm-lung contrast ($SL_{contrast}$), lung detail (L_{detail}), mediastinum detail (M_{detail}), lung noise (L_{noise}), mediastinum noise (M_{noise}), and rib-lung sharpness ($RL_{sharpness}$). In a proof of concept, the results of the IQAA were validated by 3 experienced radiologists.

Results: Regression coefficients (b) of the linear regression model indicate that the human observer results correlate well with the IQAA ($b \geq 0.89$, $R^2 \geq 0.83$). All manufacturers have SC SW that increases the 7 physical quantities of the gridless images. However, several manufacturers have SC SW that increases the physical metrics to the same level as the physical grid images. The SC SW radiographs obtained with a reduced tube load have an increased level of contrast, detail, sharpness, and noise compared with the gridless images obtained with the higher tube load.

Conclusions: We have proven in a proof of concept that the originally developed IQAA can be used to characterize different series of images of different manufacturers. Based on the physical quantities, SC SW increases the contrast, detail, sharpness, and noise. The experimental results in this study assume a patient dose reduction could be possible when SC SW is applied.

Key Words: image quality, software-based scatter correction, radiography, image quality assessment algorithm, optimization, mobile radiography unit, anthropomorphic phantom

(Invest Radiol 2022;00: 00–00)

Bedside chest radiography is one of the most commonly requested x-ray examinations in the intensive care unit (ICU), and therefore, the mobile radiography system plays an important role. Over the last few years, multiple manufacturers of mobile radiography systems have developed software to improve the image quality (IQ) of bedside radiographs—scatter correction software (SC SW)—which is intended to improve the non-scatter-corrected (gridless) images.^{1–6}

We recently reported on a study⁷ that was conducted with a contrast-detail phantom and Virtual Grid (Fujifilm, Tokyo, Japan) software where the IQ of the SC SW images could approximately be the same as the physical grid images depending on the experimental conditions. The previously cited articles/white papers conclude that SC SW improves chest radiographs and dose reduction should be possible to obtain radiographs without IQ loss. However, IQ and potential dose reduction was investigated in various manners.

Methods to assess IQ such as modulation transfer function, noise power spectrum, and detective quantum efficiency are based on simple and uniform phantoms where the preprocessed images are used to make the IQ evaluation. Besides the latter methods, contrast-detail phantoms and their evaluation can be used, although none of these methods are based on clinical images. Clinical images can be evaluated in visual grading analysis (VGA) studies, based on the quality criteria defined by the European Commission (European guidelines on quality criteria for diagnostic radiographic images). However, the latter evaluation method requires a large number of images, which have to be scored by radiologists. As a consequence, it is time-consuming and therefore not easy to implement in routine practice.^{8,9} Automated IQ evaluation of clinical radiographs can solve this difficulty. The research group of the Duke University Medical Center reported earlier on an IQAA to evaluate physical metrics, derived from the European guidelines on quality criteria for diagnostic radiographic images.¹⁰

In this study, we implemented the IQAA in our department to analyze the digital radiographs—gridless, SC SW, grid images—of 5 manufacturers of digital mobile radiography systems. The primary goal was to characterize the different series of images based on the physical metrics. Furthermore, we investigated the potential dose reduction and the correlation between the output of the physical metrics and the perceptual attributes judged by the radiologists in a proof of concept.

MATERIALS AND METHODS

Experimental Setup and Image Acquisition

Radiographs of a Lungman phantom (multipurpose chest phantom N1 “Lungman,” Kyoto Kagaku, Kyoto, Japan) were obtained with flat-panel detectors (FPDs) from 5 different manufacturers of mobile x-ray devices with the ability to turn the SC SW on and off: Agfa (Agfa Healthcare, Mortsel, Belgium), Canon (Canon Medical Systems, Shimoishigami, Japan), Fujifilm (Fujifilm, Tokyo, Japan), Philips (Philips Healthcare, Amsterdam, the Netherlands), and Samsung (Samsung Electronics Co, Seoul, South Korea). More detailed information about the detectors can be found in Table 1 (see Table,

Received for publication October 15, 2021; and accepted for publication, after revision, December 4, 2021.

From the *Department of Human Structure and Repair, Ghent University, Ghent; †Cardiovascular Center Aalst, Onze Lieve Vrouw Ziekenhuis, Aalst; ‡Department of Radiology, Ghent University Hospital, Ghent, Belgium.

Conflicts of interest and sources of funding: none declared.

Correspondence to: Tim Gossye, MSc, Department of Human Structure and Repair, Ghent University, Proeftuinstraat 86, B-9000 Ghent, Belgium. E-mail: tim.gossye@ugent.be.

Supplemental digital contents are available for this article. Direct URL citations appear in the printed text and are provided in the HTML and PDF versions of this article on the journal's Web site (www.investigativeradiology.com).

Copyright © 2022 Wolters Kluwer Health, Inc. All rights reserved.

ISSN: 0020-9996/22/0000-0000

DOI: 10.1097/RLI.0000000000000856

TABLE 1. Technical Specifications of the Different Flat-Panel Detectors

	Manufacturers				
	M1	M2	M3	M4	M5
Detector size, cm × cm				35 × 43	
Scintillator				CsI	
Detector type		Amorphous silicon with TFT		Large Area New-MIS sensor and TFT	Amorphous silicon with TFT
Pixel pitch, mm	0.148	0.150	0.148	0.125	0.140
Bit depth				12	
Settings of the SC SW	Not specified	Ratio, 13:1; lp/cm, 40; interstitial material, carbon	Not specified	Effect 5	Not specified

CsI, cesium iodide; MIS, metal insulator semiconductor; TFT, thin-film transistor; SC SW, scatter correction software.

Supplemental Digital Content 1, <http://links.lww.com/RLI/A676>, key of the pseudonymized manufacturers).

The radiographs were obtained in a controlled experimental setup on a fixed radiography system with ceiling stand and wall bucky (Siemens Ysio, Optitop 150/40/80 HC-100; Siemens; large focal spot size of 1.0 and small focal spot of 0.6), x-ray generator (Polydoros F 80-2; Siemens), and removable stationary focused grid (ratio, 13:1; lp/cm, 92; interstitial material, Al; focus-detector range, 115–180 cm). All the radiographs were obtained with the FPD inserted in the wall bucky with and without a physical grid. The source-to-image distance was set to 115 cm to mimic the source-to-image distance in daily practice on the ICU and to comply with the prescribed minimal focus-detector range of the stationary grid. The Lungman phantom was placed on the wall bucky with the backside to the FPD and with additional 3.5 cm polymethylmethacrylate (PMMA) on the chest (phantom 1). The amount of the additional PMMA (3.5 cm) was determined by analyzing the tube loads set by the automatic exposure cells (AECs) for 126 patients recorded for 1 year. These patients were all examined with the same chest x-ray protocol (anterior-posterior projection). To create more scatter, a second phantom was made with 7 cm of PMMA on the chest of the Lungman phantom (phantom 2). A tube voltage of 81 kVp was chosen to mimic the daily practice in the ICU and 125 kVp to further decrease the contrast in the radiographs. Phantom 2 was exposed to tube voltages of 81 and 125 kVp, in contrast to phantom 1, which was only exposed to 81 kVp. The tube loads were determined by the AEC (left and right chamber above the lung fields) of the radiography system without and with physical grid, dose levels 1 and 3, respectively (Table 2). Dose level 2 represents the setting that was used to expose the phantom to a reduced tube load of 11% to simulate dose reduction. The nearest tube load determined by the AEC was chosen

TABLE 2. The Different Settings That Were Used in the Experimental Setup

Dose Level	Exposure Settings	Type of Obtained Images
1	Determined on the AEC without the physical grid	Gridless/SC SW
2	Determined on the AEC ~11% mAs without the physical grid	Gridless/SC SW
3	Determined on the AEC in the presence of the physical grid	Grid

For dose level 1 and 2, 2 gridless and 2 SC SW radiographs were obtained. For dose level 3, 2 radiographs with a physical grid were obtained.

AEC, automatic exposure control; SC SW, scatter correction software.

manually in the system to make sure the same tube load was used for every manufacturer. Each x-ray exposure was repeated once, resulting in 2 images for every type of obtained image. The results of both images were averaged. Table 3 presents the tube loads and the entrance surface doses (ESDs) to which the phantoms were exposed. All presented ESDs were measured 5 times with an ionization chamber (The General Purpose, In-Beam Chamber, Radcal Corporation Model 10 × 6–6, CA, 2017), placed on the surface of the phantom in the central axis of the x-ray beam.

Image Quality Metrics and Analysis

The quality metrics, rib-lung contrast ($RL_{contrast}$), subdiaphragm-lung contrast ($SL_{contrast}$), lung detail (L_{detail}), mediastinum detail (M_{detail}), lung noise (L_{noise}), mediastinum noise (M_{noise}), and rib-lung sharpness ($RL_{sharpness}$) used in this study were previously described and validated in the study of Lin et al, Samei et al, and Willis et al.^{10–12} We implemented these quality metrics in MATLAB (MATLAB Research R2019b, the MathWorks, Inc). In contrast to Lin et al,¹⁰ regions of interest (ROIs) were manually selected on the image instead of using an automated landmark detection program. To keep the area of the ROIs (~7.6 × 7.6 mm) similar for every radiograph of the different manufacturers M1–M5, the number of pixels were adjusted, resulting in standard ROIs of 51 × 51 pixels, 61 × 61 pixels, and 54 × 54 pixels. All “for presentation” images were decomposed by a Laplacian pyramid method

TABLE 3. Description of the Used Tube Voltages and Tube Loads

Phantom	Tube Voltage, kVp	Dose Level	Tube Load, mAs	Entrance Surface Dose, mGy	Type of Obtained Images
1	81	1	0.9	0.09	Gridless/SC SW
		2	0.8	0.08	Gridless/SC SW
		3	2.8	0.30	Grid
2	81	1	1.8	0.20	Gridless/SC SW
		2	1.6	0.17	Gridless/SC SW
		3	6.3	0.72	Grid
2	125	1	0.71	0.14	Gridless/SC SW
		2	0.63	0.12	Gridless/SC SW
		3	1.6	0.38	Grid

Detailed information about the exposure parameters to irradiate the 2 phantoms. Entrance surface doses are the average of 5 repeats.

kVp, kilovoltage peak; mAs, milliampere-seconds; mGy, milligray; SC SW, scatter correction software.

into 5 frequency subbands to separate the high-frequency noise and low-frequency signal.^{10,13}

Lung Gray Level, Lung Detail, and Lung Noise

Six standard-sized ROIs were placed in the lungs: 3 ROIs in the left and 3 ROIs in the right lung (Fig. 1).

The lung gray level $L'_{graylevel}$, averaged over the 6 ROIs, is determined using the following formula:

$$L'_{graylevel} = \frac{1}{6} \sum_{i=1}^6 Mean(L_i) \quad (1)$$

where $Mean(L_i)$ is the mean pixel value of each lung ROI.

After decomposing the image into 5 digressive frequency subbands by the Laplacian pyramid method, detail and noise are calculated respectively as follows:

$$L_{detail} = \frac{1}{6} \sum_{i=1}^6 Std(L_i \text{ in subband } 3) \quad (2)$$

$$L_{noise} = \frac{1}{6} \sum_{i=1}^6 Std(L_i \text{ in subband } 0) \quad (3)$$

where $Std(L_i)$ is the standard deviation of the mean pixel value of each lung ROI in subband 3 and 0 for L_{detail} and L_{noise} , respectively.

Mediastinum Detail and Mediastinum Noise

Ten ROIs, double the size of the standard ones, were placed on the spine above the diaphragm (Fig. 1). Similar to the description of the previous paragraph, detail and noise parameters of the mediastinum are calculated as follows:

$$M_{detail} = \frac{1}{10} \sum_{i=1}^{10} Std(M_i \text{ in subband } 3) \quad (4)$$

$$M_{noise} = \frac{1}{10} \sum_{i=1}^{10} Std(M_i \text{ in subband } 0) \quad (5)$$

where $Std(M_i)$ is the standard deviation of the mean pixel value of each mediastinum ROI in subband 3 and 0 for M_{detail} and M_{noise} , respectively.

Rib-Lung Contrast

Six standard-sized ROIs, mentioned previously, were placed on rib edges (Fig. 1): 3 ROIs in the left and 3 ROIs in the right lung. $RL_{contrast}$ can be calculated in each ROI as follows:

$$RL_{contrast} = \max_{i=1,2,\dots,8} \left\{ \frac{2 \cdot |W * F_i|}{W * |F_i|} \right\} \quad (6)$$

where W is the image ROI and F_i is 1, 2, ..., 8 directional contrast filters that were developed to automatically detect ROIs on the rib edges. The filters apply a directional splitting line (zero value elements), dividing each filter into a +1 region and a -1 region.¹⁰ The convolution term $|W * F_i|$ calculates the absolute difference of the summation of the 2 regions, whereas the convolution term $W * |F_i|$ calculates the sum of the whole ROI, except for the pixels coinciding with the filter's splitting line.¹⁰ The filter F_i , resulting in the maximum $RL_{contrast}$, is retained and used to calculate the gray levels of both structures present in the ROI. The orientation of the latter filter corresponds closely with the ROIs rib-edge orientation. Because the $RL_{contrast}$ can traditionally be defined as follows:

$$RL_{contrast} = \frac{2 \cdot (R_{graylevel} - L''_{graylevel})}{R_{graylevel} + L''_{graylevel}} \quad (7)$$

we can compute the ribs and part of the lungs' gray level as follows:

$$R_{graylevel} = (W * |F_i| + |W * F_i|) / N \quad (8)$$

$$L''_{graylevel} = (W * |F_i| - |W * F_i|) / N \quad (9)$$

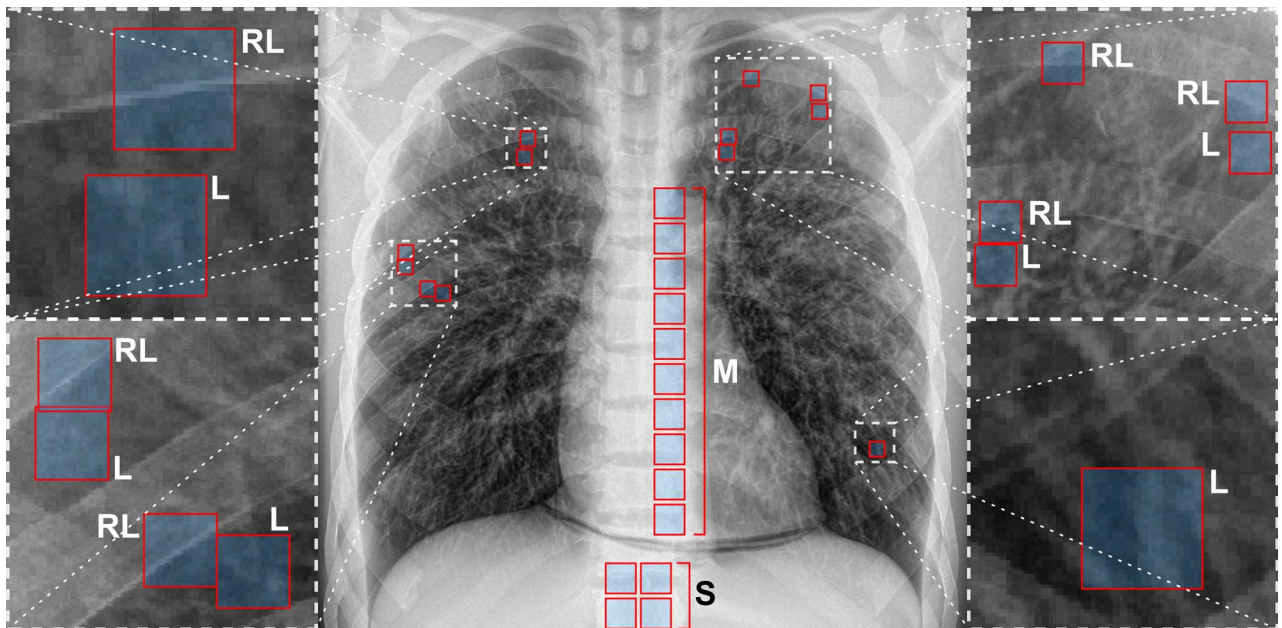


FIGURE 1. Position of the ROIs for the different regions in the radiographs. RL and S ROIs were used to calculate the $RL_{contrast}/RL_{sharpness}$ and $SL_{contrast}$ respectively. L ROIs and M ROIs were used to calculate L_{detail} , L_{noise} and M_{detail} , M_{noise} respectively. ROIs, region of interest; RL, rib-lung; S, subdiaphragm; SL, subdiaphragm-lung; L, lung; M, mediastinum.

where N is the ROI size that was used on the images (excluding the zero matrix elements). Eventually, $RL_{contrast}$ is averaged over all 6 ROIs.

Subdiaphragm-Lung Contrast

The 4 subdiaphragm ROIs were positioned below the diaphragm along the spine and are double the size of the aforementioned standard ROIs (Fig. 1). To determine the $SL_{contrast}$, we need to determine the subdiaphragm gray level ($S_{graylevel}$) and L gray level ($L_{graylevel}$) first. $S_{graylevel}$ is defined as the average of the ROI mean pixel values:

$$S_{graylevel} = \frac{1}{4} \sum_{i=1}^4 Mean(S_i) \quad (10)$$

where $Mean(S_i)$ is the mean pixel value of each subdiaphragm ROI.¹⁰

Because both the lung and rib-lung ROIs contain lung tissue, $L_{graylevel}$ is determined as a weighted sum of, on the one hand, $L'_{graylevel}$ —the mean gray level of the pixels confined by the ROIs only consisting of lung tissue (averaged over all 6 lung ROIs) (1)—and on the other hand, $L''_{graylevel}$ —the mean gray level of the lung tissue pixels confined by the ROIs positioned on the rib-lung edges (9). Eventually, $L_{graylevel}$ is calculated according to the following formula:

$$L_{graylevel} = \frac{1}{3} (2L'_{graylevel} + L''_{graylevel}) \quad (11)$$

Now that we have obtained both the $L_{graylevel}$ and $S_{graylevel}$, we compute the $SL_{contrast}$ according to the following equation¹⁰:

$$SL_{contrast} = \frac{2 \cdot (S_{graylevel} - L_{graylevel})}{S_{graylevel} + L_{graylevel}} \quad (12)$$

Rib-Lung Sharpness

The same standard-sized ROIs that were used to calculate the $RL_{contrast}$ are used to calculate the $RL_{sharpness}$ (Fig. 1). Similar to the article of Lin et al,¹⁰ each 3-pixel-wide column was averaged to reduce the quantum and structure noise while maintaining the profile of the rib shape. On the averaged profile, a 30-pixel window was slid down from rib side to lung side (top to bottom). The 30-pixel window resulting in the largest difference between the maximum and minimum pixel values of the profile was retained. The latter profile was preprocessed to further reduce large variations while maintaining the main edge characteristics¹⁰ before fitting a sigmoid function according to equation (13):

$$f_{sigmoid}(x) = a + \frac{b}{1 + e^{\frac{x-a}{\sigma}}} \quad (13)$$

Finally, the first derivative at the inflection point of the fitted sigmoid is applied as the definition of RL sharpness for profile i and ROI j :

$$RL_{sharpness(i,j)} = \arctan\left(\left|\frac{b}{4d}\right|\right) \quad (14)$$

Eventually, the values obtained for each 3-column-averaged profile in each ROI are averaged to obtain the final $RL_{sharpness}$.¹⁰

Image Evaluation by the Human Observers

In the proof of concept, 2 tasks were performed to compare the gridless images with the SC SW images. The comparisons were made for the radiographs of the Lungman phantom +7 cm PMMA exposed to 125 kVp (0.71 mAs), as these radiographs should be the most affected by the scattered x-rays (high tube voltage and thickest phantom in the experimental setup).

All quality metrics from the IQAA were evaluated separately by 3 experienced abdominal-thoracic radiologists (35 years, 8 years, and

7 years of experience). All the images were presented in an anonymized form to the radiologists on a 30-inch 6 MP Barco screen (model: Coronis Fusion; Barco NV, Kortrijk, Belgium), which was configured in 2×3 MP.

The first task for the radiologists was to evaluate which of the images—gridless versus SC SW—displayed superior visibility of the different structures of interest (structure i). The structures of interest were the following: lung parenchyma (corresponds to L_{detail}/L_{noise}), the spine behind the mediastinum (corresponds to M_{detail}/M_{noise}), rib-lung edges to evaluate $RL_{sharpness}/RL_{contrast}$ and subdiaphragm-lung region to evaluate the $SL_{contrast}$. The subdiaphragm region was explained as the area below the diaphragm where the spine is situated. Images were displayed side by side, without informing the radiologists which side displayed which image (gridless or SC SW) (Fig. 2).

The second task was to rank the (anonymized) manufacturers according to the observable differences between gridless and SC SW images from largest (=1) to smallest (=5) difference, again showing the images side by side for each manufacturer separately. For the latter task, the observer was able to return to previous image pairs whenever desired. In this way, it was possible to make a ranking from small to large difference between the images, for example, the difference between the SC SW image and gridless image of manufacturer A is larger than the difference between the SC SW image and gridless image of manufacturer B, and so on (Fig. 2). Regarding the IQAA, image differences are quantified for each structure and physical parameter as the ratio of the parameters value in the SC SW image and its corresponding value in the gridless image, expressed in %.

Statistical Analysis

To assess the relationship between the results of the IQAA and the human observers, we fitted a linear regression model through the origin of the graph. The parameter estimate b ($y = b \times x$) was calculated, and the goodness-of-fit of the models was evaluated with R^2 . Results are considered significant when P values < 0.05 . All analyses were done with Statistical Package for Social Sciences (IBM Corp Released 2017, IBM SPSS Statistics for Windows, Version 25.0; IBM Corp, Armonk, NY).

RESULTS

Image Evaluation by the Human Observers

For the first assignment, the human observers indicated that all the structures of the SC SW images are more visible than the structures of the gridless images. This is in agreement with the values of the metrics calculated by the IQAA, which are larger in the SC SW images. In Figure 3, the averaged human observer ranking is plotted against the IQAA ranking. A good fit is made for the structures contrast, detail, and sharpness ($b \geq 0.97$ and $R^2 \geq 0.95$ with $P < 0.01$). Noise structures correlate less with $b \geq 0.89$ and $R^2 \geq 0.83$ ($P < 0.05$). More deviations among the human observers are seen in the ranking of these structures, which indicates that less interobserver agreement was met. The latter is also observed, expressed by a larger standard deviation, when smaller observable differences (higher ranks) in the images are noticed.

Comparisons of the SC SW Images to Gridless and Grid Images

Figure 4 represents the comparisons between gridless radiographs, SC SW radiographs, and radiographs obtained with a grid inserted in the bucky (grid images) (Lungman phantom +7 cm PMMA, exposed to 125 kVp) (see Table, Supplemental Digital Content 2, <http://links.lww.com/RLI/A677>, raw data of the IQAA). Compared with the gridless images, the highest values of contrast, sharpness, and detail are observed in the grid images. Noise values of the grid images are more or less similar to the ones from the gridless images. All manufacturers have SC SW that increases contrast, detail, sharpness, and noise levels

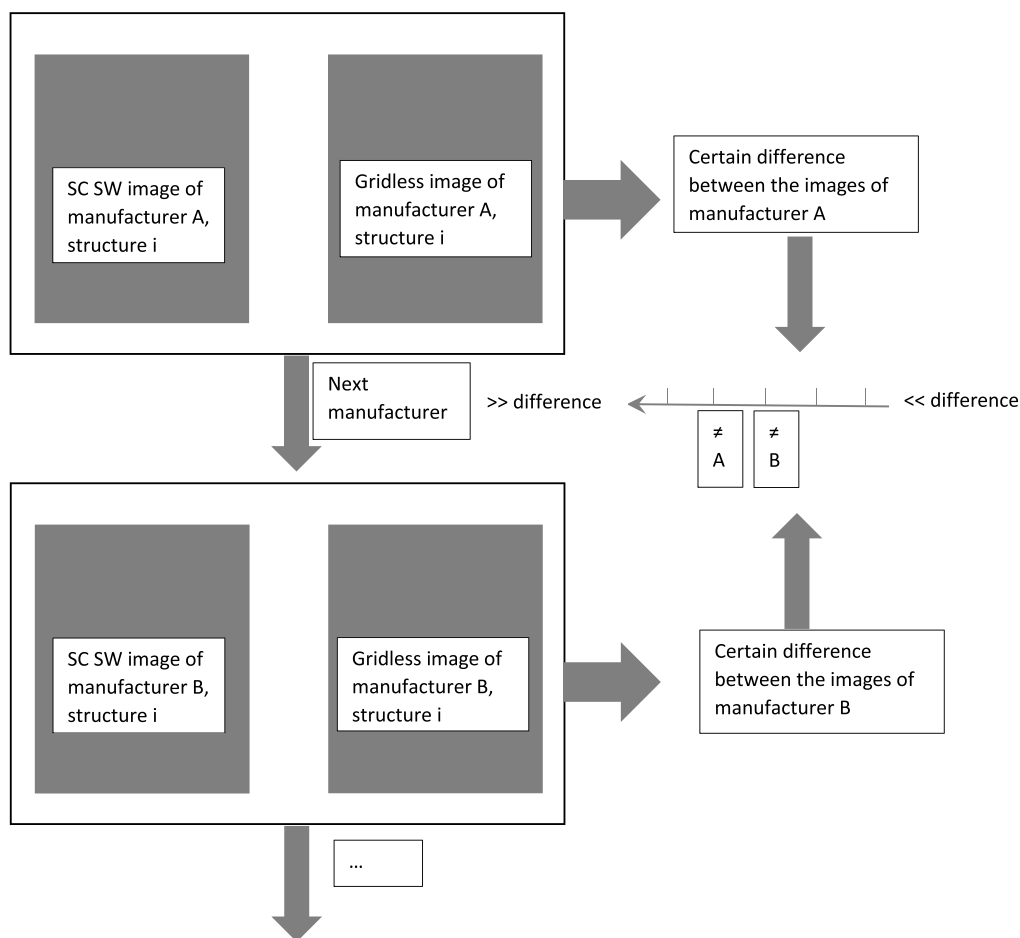


FIGURE 2. A schematic view of the workflow to compare the differences between gridless images and SC SW images. SC SW, scatter correction software.

above the level of the gridless images, but some obtain even higher values with the SC SW images than with the grid images.

The SC SW radiographs of the manufacturers M1, M2, and M5 contain more $RL_{contrast}$, L_{detail} , and noise values than the grid radiographs. Considering $SL_{contrast}$ and M_{detail} , only manufacturer M2 has more contrast and detail in the SC SW images than in the grid images.

Of all manufacturers, M2–M4 SC SW radiographs have smaller noise values. However, contrast and detail levels are smaller as well, except for M2. Sharpness values are lower in the radiographs that were obtained with FPDs with pixel size of 0.125 mm and 0.140 mm, respectively, manufacturer M4 and M5.

Potential Dose Reduction of SC SW (IQAA)

In Figure 4, we observed that applying SC SW increases the contrast, sharpness, detail, and noise. The increased values of contrast, sharpness, and detail caused by the SC SW suggest the possibility to lower the tube load, considering noise increases with lower tube loads. Results of the decreased tube load with 11% are presented in Figure 5 (0.71 mAs vs 0.63 mAs) (see Table, Supplemental Digital Content 2, <http://links.lww.com/RLI/A677>, raw data of the IQAA). Values of the quality metrics of the SC SW images obtained with the lower tube load are compared with the values of the gridless images with the initially higher tube load.

Compared with the gridless images, values are higher when SC SW is applied to the images, even with a lower tube load. $SL_{contrast}$ of manufacturer M3 and M4 radiographs does not improve above the level of the gridless images.

Comparison of the SC SW Images to Gridless and Grid Images of the Other Experimental Setups

Results of the phantom +7 cm PMMA exposed to 81 kVp (see Table, Supplemental Digital Content 3, <http://links.lww.com/RLI/A678>, raw data of the IQAA) are similar to the earlier described results with 125 kVp (see Table, Supplemental Digital Content 2, <http://links.lww.com/RLI/A677>, raw data of the IQAA). The tube load, based on the AEC of the fixed radiography system, to obtain gridless/SC SW images, was determined on 1.8 mAs, 2.5 times more than with 125 kVp. The tube load to obtain the grid images was 3.9 times higher than the tube load used to obtain the grid images with 125 kVp.

According to the IQAA, the images obtained with 81 kVp contain in general more contrast, sharpness, and detail than the images obtained with 125 kVp. Noise levels are similar.

Compared with the gridless images, the grid images contain in general more contrast, sharpness, and detail. Noise levels of the grid images are similar to those in the gridless images. SC SW increases the values of the quality metrics of the gridless images.

When we look at the results of the Lungman +3.5 cm exposed to 81 kVp (see Table, Supplemental Digital Content 4, <http://links.lww.com/RLI/A679>, raw data of the IQAA), we observe results similar to our Lungman +7 cm phantom exposed to 81 kVp. The tube load to obtain our images was 0.9 and 2.8 mAs (based on AEC of the fixed radiography system) for gridless/SC SW and grid images, respectively. Contrast, sharpness, and detail are higher in grid images than in gridless images. L_{Noise} levels of the grid images are similar to those in the

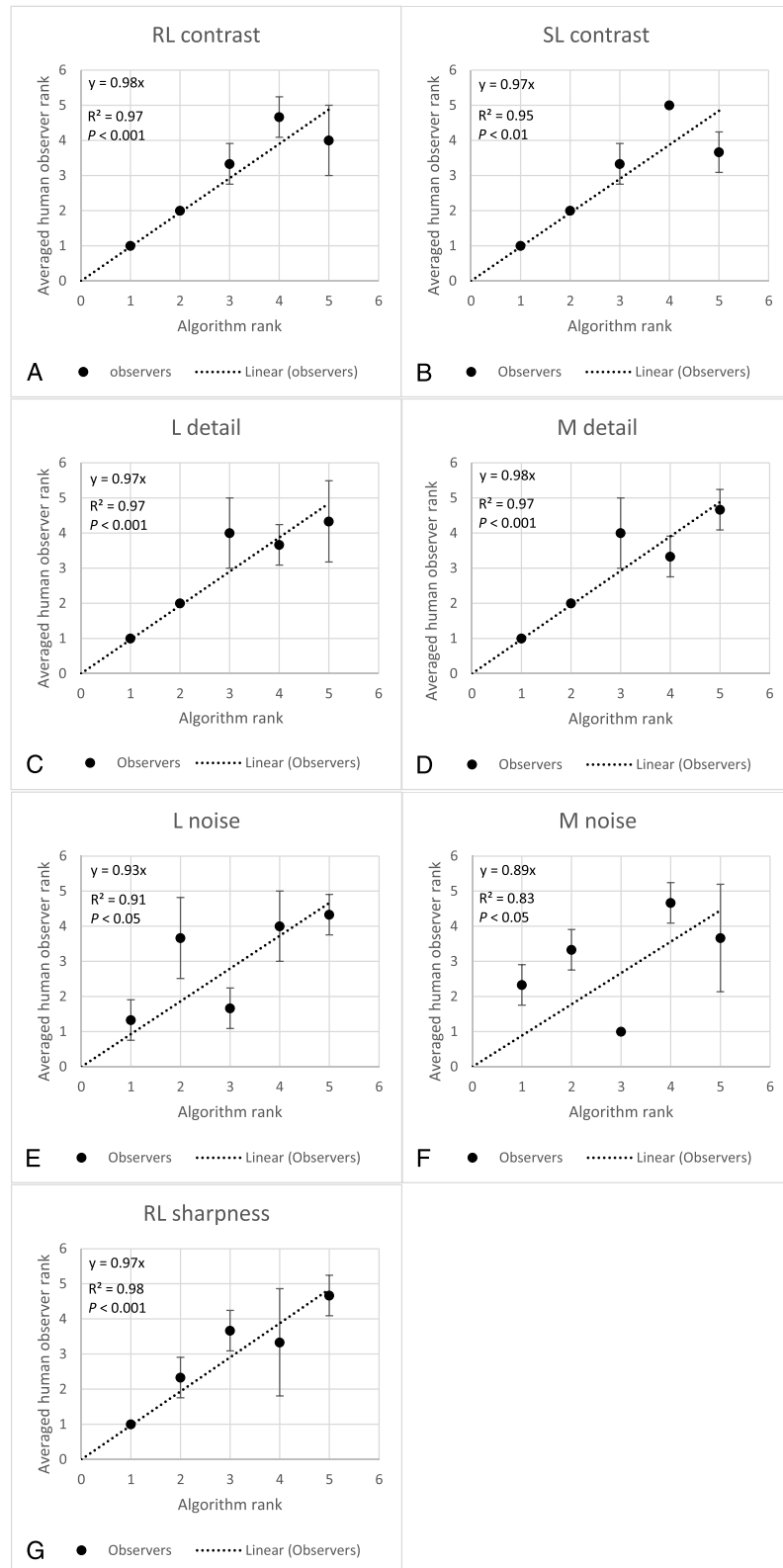


FIGURE 3. A–G, Results of plotting the rankings of the averages of the human observer and the IQAA rankings. For each structure, a linear fit (dashed line) through 0 is modeled, and the regression coefficient b ($y = b \times x$) is calculated to express the relationship between the human observers and the IQAA ranks. In each graph, the R^2 of the models and the P values are presented. RL contrast, rib-lung contrast; SL contrast, subdiaphragm-lung contrast; L detail, lung detail; M detail, mediastinum detail; L noise, lung noise; M noise, mediastinum noise; RL sharpness, rib-lung sharpness; IQAA, image quality assessment algorithm.

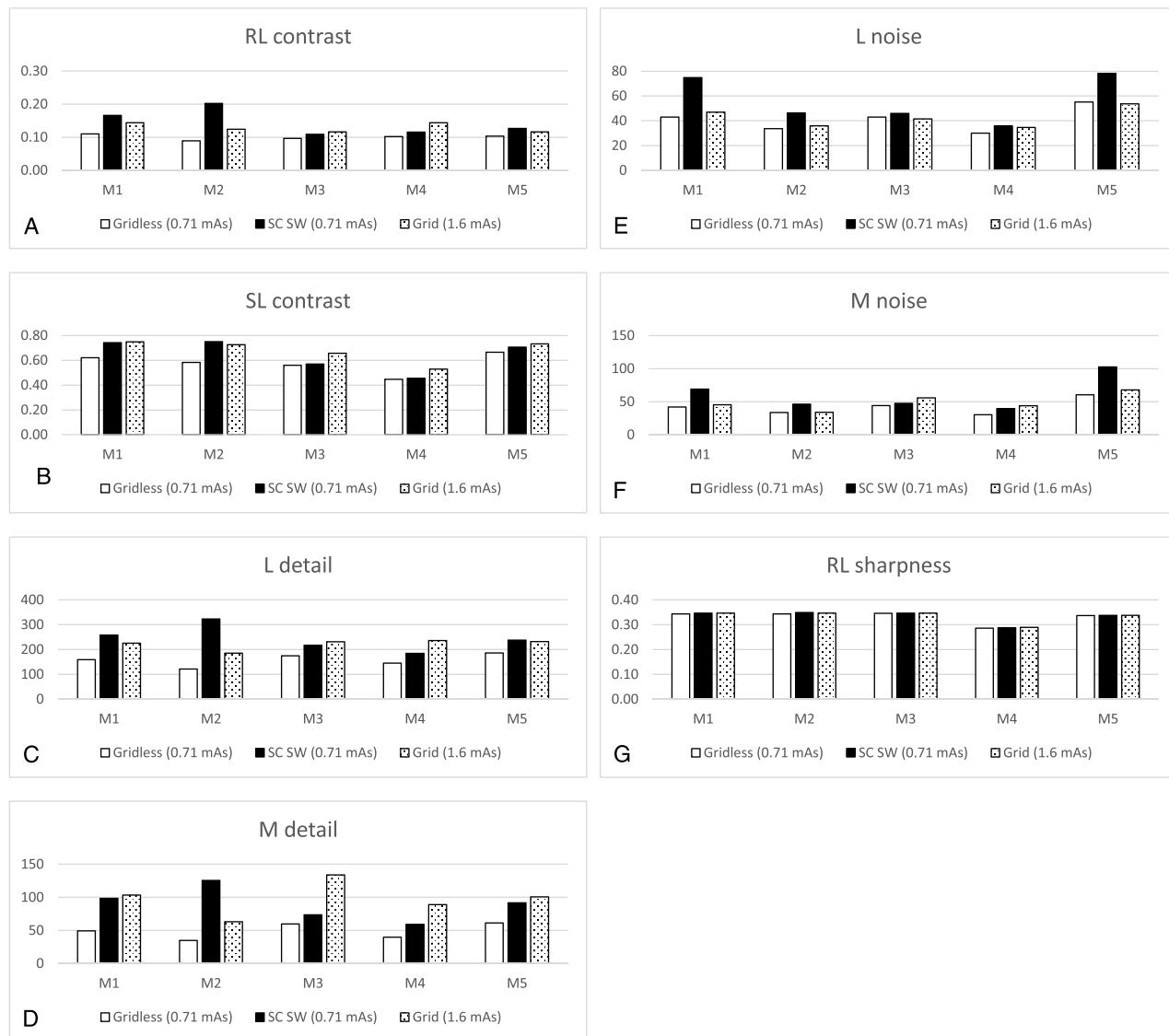


FIGURE 4. A–G, Values of the quality metrics contrast, detail, noise, and sharpness obtained with the Lungman phantom with 7 cm of added PMMA and exposed to 125 kVp for gridless, SC SW images, and grid images. Gridless and SC SW images were obtained with 0.71 mAs. Grid images were obtained with 1.6 mAs. RL contrast, rib-lung contrast; SL contrast, subdiaphragm-lung contrast; L detail, lung detail; M detail, mediastinum detail; L noise, lung noise; M noise, mediastinum noise; RL sharpness, rib-lung sharpness; SC SW, scatter correction software.

gridless images. Just like with the 2 other experimental setups, SC SW increases the values of the quality metrics of the gridless images. The images acquired with the thinner phantom show more contrast, sharpness, and detail than the images acquired with the Lungman +7 cm phantom.

The results of the dose reduction on the Lungman phantom +7 cm PMMA, exposed to 125 kVp, are similarly applicable to the 2 other experimental setups. When we reduce the tube load by 11% and apply SC SW, all values of the quality metrics are still higher compared with the values of the gridless images obtained with the higher tube load.

DISCUSSION

Mobile radiography systems are often used in bedside chest imaging in the follow-up of critically ill patients. The IQ of radiographs obtained at bedside is often compromised because of the lack of use of the physical scatter rejection grid. Because the first SC SW applications were released in 2015, multiple SC SW products have become available

to improve the IQ of bedside gridless images.⁷ To our knowledge, no studies of intercomparisons of different mobile radiography systems with the possibility to apply such software on the images have been published.

Although all the radiographs of the different manufacturers were obtained in the same conditions and judged as diagnostically acceptable, each manufacturer has its own way of visually presenting the image. In this way, objective scoring is more difficult.

One of the methods to investigate the IQ is with a VGA study. However, the latter is time-consuming and puts an extra workload on the radiologists. Therefore, we implemented a computational method—IQAA—in our department to characterize the clinical radiographs. This method was previously developed and validated on patient images by the Duke University Medical Center in the studies of Lin et al, Samei et al, and Willis et al with good agreement with human observers.^{10–12}

In our study, good linear regression models were obtained for the structures contrast, detail, and sharpness but lesser for the structures

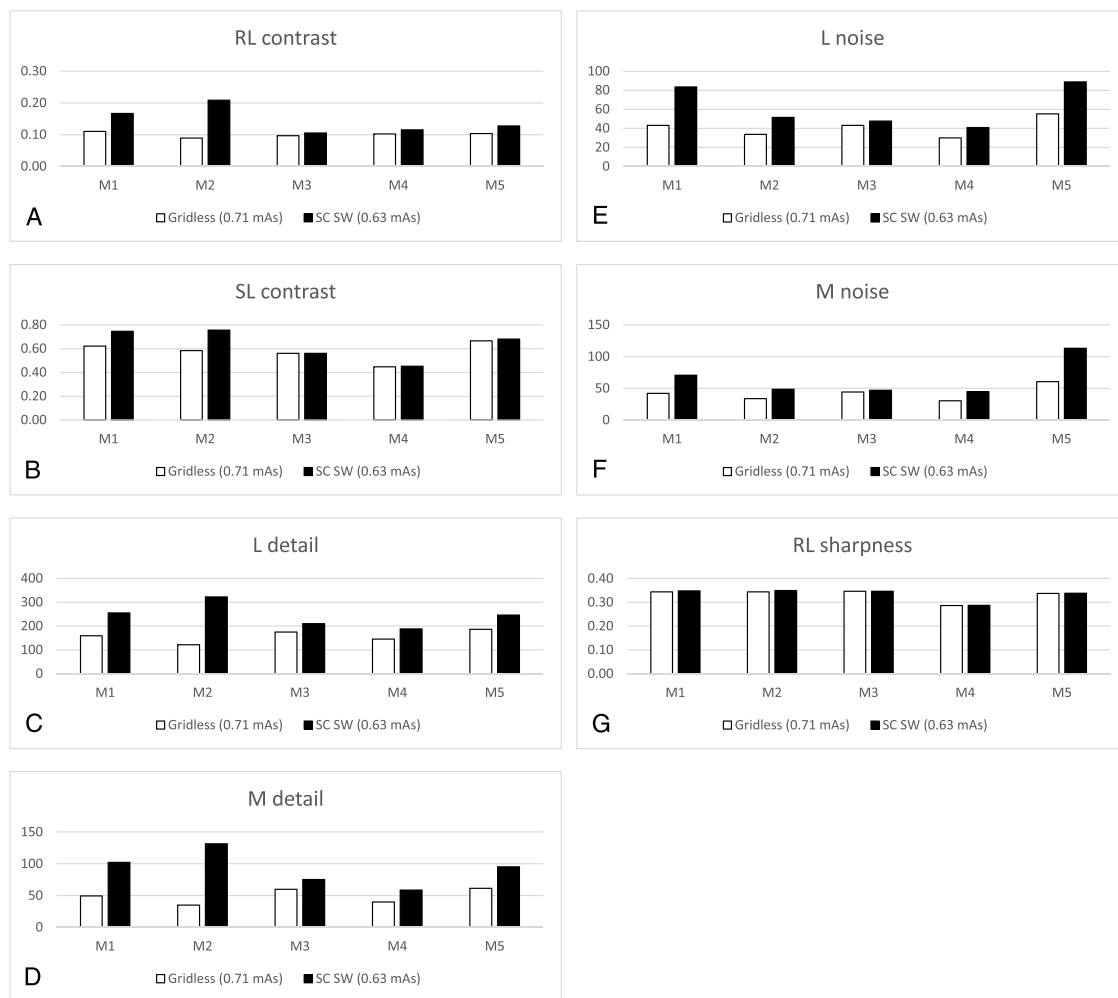


FIGURE 5. A–G, Values of the quality metrics contrast, detail, noise, and sharpness obtained with the Lungman phantom with 7 cm of added PMMA and exposed to 125 kVp. Values of the quality metrics are shown for gridless images obtained with 0.71 mAs and SC SW images obtained with 0.63 mAs (11% dose reduction). RL contrast, rib-lung contrast; SL contrast, subdiaphragm-lung contrast; L detail, lung detail; M detail, mediastinum detail; L noise, lung noise; M noise, mediastinum noise; RL sharpness, rib-lung sharpness; SC SW, scatter correction software.

lung and mediastinum noise. The latter observation can be attributed to the little amount of noise in the images as detected by the radiologists. Nevertheless, regression coefficients and R^2 were higher than 0.89 and 0.83, respectively.

Our study was conducted with a Lungman phantom with additional PMMA to increase the scatter level in the image. However, some anatomical structures in the phantom are more visible on the radiographs than in patients radiographs, for example, pulmonary blood vessels in the lung (L_{detail}). This results in a quality metric L_{detail} of 122–186 for gridless images obtained with our Lungman phantom +7 cm, 125 kVp, and 0.71 mAs. In the studies of Lin et al and Samei et al,^{10,11} L_{detail} levels ranged from ~10 to ~40. As they explain in their studies, the radiographs were chosen to cover a broad range of values and in such a way to maintain largely equidistant intervals between the values of the quality metrics. With our experimental setup, it was not possible to maintain equidistant intervals in the values of the quality metrics between the radiographs.

SC SW increases the quality metrics contrast, detail, noise, and sharpness of the gridless images of all 5 manufacturers. However, not all quality metrics of all manufacturers reached the same high level as in the grid images. This is mostly noticed in the SC SW images of manufacturer M3 and M4 for all the quality metrics, except M_{noise} .

As for the radiographs of manufacturer M1 and M5, the physical grid is more beneficial for the metrics noise, $SL_{contrast}$ and M_{detail} . However, the tube load that was used to obtain the grid images was more than 2 times higher than the tube load to obtain the SC SW images.

All manufacturers were informed about the physical grid specifications (ratio, 13:1; lp/cm, 92; interstitial material, Al) and were asked to adjust the SC SW settings to a similar level as the physical grid when possible. Manufacturer M2 is the only manufacturer with this ability and where the SC SW quality metrics exceeded the level of the physical grid quality metrics, except for noise. Similar results were found in our former article⁷ where SC SW was able to outperform the physical grid, but ESDs were kept identical to obtain the physical grid and SC SW radiographs. The remaining manufacturers could not adjust the settings of the SC SW or chose the standard settings, which may explain the differences between the SC SW and grid images. The effects on the IQ of changing the SC SW grid ratio is also described in our former article.⁷ Further research should be performed to investigate if our current results are applicable to other grid characteristics.

Based on our results of increased contrast, detail, and sharpness, a potential patient dose reduction can be assumed when SC SW radiographs are compared with the gridless radiographs. Despite the limited tube load reduction of 11%, it can still be of value. According to the

studies of Delnevo et al and Wu et al,^{14,15} patients undergo multiple x-ray examinations during their stay in the ICU, emphasizing the importance of a potential dose reduction. The potential dose reduction in the articles/white papers^{1-3,5,6} focuses mainly on the dose difference between SC SW radiographs and physical grid radiographs. As a consequence, the reported potential dose reduction is often larger in these articles than 11%.

One of the limitations in the current study is that we did not investigate what the general IQ is of the radiographs like in VGA studies. However, in the current experimental setup, we believe that the IQAA used in this study provides more objective results than human observers scoring images from different manufacturers. A second limitation of the study is the small group of radiologists that were evaluating the differences between the radiographs. A different group of radiologists could provide different results, but in the current study, our results show good correlation between the radiologists and IQAA, and are in line with the results of Lin et al.¹⁰

In summary, in the current anthropomorphic phantom study, we investigated the effects of SC SW on different quality metrics that were previously developed by the Duke University Medical Center. Good correlations between the human observers and the IQAA were found. All manufacturers have SC SW that improve contrast, detail, and sharpness. However, noise increases as well. Nevertheless, differences among the manufacturers exist. Some manufacturers allow to change the settings of the software applications and could explain the differences. With the increased quality metrics, we are able to suggest reducing the tube load, but it remains unclear what the effect is of the increased noise on the general IQ. More research should be performed to investigate this.

REFERENCES

1. Canon. Scatter Correction Excellent image contrast without a grid.
2. Kawamura T, Naito S, Okano K, et al. Improvement in image quality and workflow of x-ray examination using a new image processing method, "virtual grid technology". *Imag Technol Center*. 2014.
3. Lee B, Song J, Kim D, et al. Improving the image quality with a novel software-based scatter correction: SimGrid™ Technology. 2017.
4. Precht H, Morup SD, Tingberg A, et al. Can scatter correction software replace a grid in dr pelvic examinations? *Radiat Prot Dosimetry*. 2019;187:8–16.
5. Renger B, Brieskorn C, Toth V, et al. Evaluation of dose reduction potentials of a novel scatter correction software for bedside chest x-ray imaging. *Radiat Prot Dosimetry*. 2016;169(1–4):60–67.
6. Verstreepen L, Wanninger F, Apgar B. Non-grid bedside chest imaging. 2016.
7. Gossye T, Smeets PV, Achten E, et al. Impact of software parameter settings on image quality of virtual grid processed radiography images: a contrast-detail phantom study. *Invest Radiol*. 2020;55:374–380.
8. De Crop A, Bacher K, Van Hoof T, et al. Correlation of contrast-detail analysis and clinical image quality assessment in chest radiography with a human cadaver study. *Radiology*. 2012;262:298–304.
9. European Commission. *European Guidelines on Quality Criteria for Diagnostic Radiographic Images (EUR 16260 EN)*. Luxembourg: Office for Official Publications of the European Communities; 1996.
10. Lin Y, Luo H, Dobbins JT, et al. An image-based technique to assess the perceptual quality of clinical chest radiographs. *Med Phys*. 2012;39:7019–7031.
11. Samei E, Lin Y, Choudhury KR, et al. Automated characterization of perceptual quality of clinical chest radiographs: validation and calibration to observer preference. *Med Phys*. 2014;41:111918.
12. Willis CE, Nishino TK, Wells JR, et al. Automated quality control assessment of clinical chest images. *Med Phys*. 2018;45:4377–4391.
13. Burt PJ, Adelson EH. The Laplacian pyramid as a compact image code. *IEEE Trans Commun*. 1983;31:532–540.
14. Delnevo A, Tritella S, Carbonaro LA, et al. The use of bedside chest radiography at a university hospital. Data on a two-week period. *Eur J Radiol*. 2012;81:e260–e263.
15. Wu G, Li X. Mobile x-rays are highly valuable for critically ill COVID patients. *Eur Radiol*. 2020;30:5217–5219.